48th AIAA/ASME/ASCE/AHS/ASC Structures, Structural Dynamics, and Materials Conference
 15th
23 - 26 April 2007, Honolulu, Hawaii

AIAA 2007-2308

AIAA/ASME/ASCE/AHS/ASC 48^{th} Structures, Structural Dynamics, and Materials Conference, April 23-26 2007, Honolulu, HI

A Macroscopic Finite Element for a Symmetric Double Lap Joint Subjected to Mechanical and Thermal Loading

Peter A. Gustafson*, Anthony M. Waas†

Department of Aerospace Engineering,University of Michigan,Ann Arbor, MI 48109, USA

A thermo-mechanical analytical model and a corresponding macroscopic bonded joint finite element is presented for the analysis of orthotropic double lap joints subjected to combined thermal-mechanical loads. The analytical solution offers an improvement in accuracy over its predecessor,[1,2] at the cost of increased solution complexity. However, to facilitate the use of this solution, it has been incorporated into a macroscopic bonded joint finite element.[3] The single element reproduces the analytical solution with minimal analyst input, and therefore can be easily incorporated into early design studies. The macroscopic element provides a computationally efficient and mesh independent comparative stress result. To validate the element, the stress predictions of the single element are compared with a continuum finite element model.

Nomenclature

l_e	Length of the lap sub-element, m
t_κ	Material thicknesses of component κ, m
x,y	Cartesian coordinates measured from the lower left corner of the adhesive, m
$\sigma_{\kappa 11(x)}$	Longitudinal stress in component κ, Pa
$\sigma_{\kappa 22(x,y)}$	Transverse stress in component κ, Pa
$\tau_{\kappa 12(x)}$	Shear stress in component κ, Pa
$\hat{\sigma}_{\kappa 11(x)}$	Longitudinal virtual stress in component κ
$\hat{\sigma}_{\kappa 22(x,y)}$	Transverse virtual stress in component κ
$\hat{\tau}_{\kappa 12(x)}$	Shear virtual stress in component κ
$E_{\kappa ii}$	Orthotropic engineering moduli of component κ, Pa
G_{bij}	Orthotropic shear modulii of the adhesive, Pa
$\alpha_{\kappa ii}$	Orthotropic thermal expansion coefficient of component κ, $^\circ\mathrm{C}^{-1}$
$\nu_{\kappa ij}$	Poisson's ratios of component κ
P	Mechanical load applied to the joint, per unit depth, N m^{-1}
P_1,P_2	Element internal mechanical load DOFs, per unit depth, N m^{-1}
ΔT	Temperature change from a reference temperature, $^\circ$C
$\bar{x}$	Normalized coordinate $\frac{x}{l_e}$ measured from the left edge of the joint
$\bar{\beta}$,$\bar{\gamma}$,$\bar{\lambda}_1$,$\bar{\lambda}_3$	Dimensionless system parameters
$\bar{\phi}_P$	Dimensionless mechanical load parameter
$\bar{\phi}_T$	Dimensionless thermal load parameter
$\bar{\phi}_{total}$	Dimensionless total load parameter
$\bar{\phi}_P$	Dimensionless mechanical load fraction
$\bar{\bar{A}}, \bar{\bar{B}}, \bar{\bar{C}}, \bar{\bar{D}}$	Dimensionless basis coefficients

*Graduate Student Research Assistant. Member AIAA. email: petegus@umich.edu

†Professor. Associate Fellow, AIAA. Corresponding author, email: dcw@umich.edu

$\bar{\bar{\Phi}}_a, \bar{\bar{\Phi}}_c$	Intermediate variables
$\bar{\bar{\Xi}}_a, \bar{\bar{\Xi}}_c$	Intermediate variables
q_1, q_2, q_3, q_4	Nodal displacement degrees of freedom
q_e	Subelement extension degree of freedom
N_a, N_c	Element shape functions
B_a, B_c	Element shape function derivatives

Subscripts

[]	the *or* operator, i.e. [12] is 1 *or* 2 (no sum)
κ	$\kappa = [abcp]$ (no sum) Subscript representing central adherend (a), adhesive (b), outer adherend (c), and end post (p) respectively
ii	$i = [123]$ (no sum)
ij	$i, j = [123]$ where $i \neq j$ (no sum)

I. Introduction

RECENT advances in structural epoxies and adhesives have expanded the temperature range over which high performance fibrous composite materials can be used. In the structures composed of these materials, adhesively bonded joints are widely used due to improved load distribution, increased service life, reduced machining cost, and/or reduced complexity.[4] These epoxies and adhesives, designed to provide structural integrity at high temperature, are subjected to severe operating environments. Furthermore, manufacturing processes subject these materials to broad temperature ranges during the different stages of the curing cycle. It is known that high stress gradients can exist near the edges of bonded joints due to mismatches in thermal expansion coefficients and elastic moduli.[5] Therefore, components made from these materials carry a significant risk of adverse stress caused by differential thermal expansion, even when used at room temperature. Due to the increased use of composite materials and bonded joints, the need for efficient and effective thermo-mechanical analysis tools is greater than ever.

The design and modeling of bonded joints is not yet a mature field. Continuum finite element (FE) models of adhesively bonded joints are widely available in the literature, where work began as early as 1971 (Wooley and Garver,[6] and Adams and Peppiatt[7] are early references). More recently, promising advances in cohesive zone (including Kafkalidis and Thouless,[8] Xie et al.,[9] Li et al.,[10,11] Valoroso and Champaney[12]), discrete cohesive zone (Xie et al.[13]), fracture mechanics (Weerts and Kossira[14]), probabilistic prediction (Aydemir and Gunay,[15] Koutsourelakis et al.[16]), virtual crack closure (including Gillespie et al.,[17] Wang et al.,[18] Glaessgen et al.,[19] Krueger,[20] Xie et al.[21–23]), and other adhesive region models (including Munoz et al.,[24] Goncalves et al.,[25] Goyal et al.[26]) have greatly increased the predictive capability of FE techniques. Cohesive zone models have been incorporated into commercial software, including Abaqus®,[27] as well as freely available research codes like Tahoe®.[28] However, despite their availability, the listed techniques are expensive and require user expertise. Therefore there are ongoing efforts to develop rapid analysis techniques (Oterkus et al.,[29,30] Smeltzer and Lundgren[31]), a key enabling technology for vehicle designers.

Though models built with the tools listed above can be accurate and very capable, they rely on the presence of a meshed joint, where continuum elements represent the adherends, and the adhesive is represented by continuum elements or a discrete traction separation law. There is significant overhead in creating and analyzing joints using these and other continuum numerical methods. Mesh generation and manipulation is an obstacle for all but academic geometries. Mesh density is also a consideration, since the computational time for basic joints can be significant if non-linear material properties and material degradation criterion are included. As a result, there are ongoing efforts to evaluate analysis techniques that are less mesh dependent. For example, the Composites Affordability Initiative has recommended a p-based analysis code for analysis of adhesively bonded joints.[a] Use of p-based codes should be less mesh dependent than the more commonly used h-based FE codes. Similarly, Bednarcyk et al.[32] used a higher order, semi-analytical theory (developed for functionally graded materials) to analyze a double lap and a bonded doubler joint. This technique was reported to be less mesh dependent than h-based analysis methodologies.

Although the techniques cited above attempt to minimize mesh dependency, they do not eliminate it. Due to mesh generation overhead and computational cost, it is often impractical and sometimes impossible

[a] http://www.esrd.com [cited Feb. 2007]

to include joint models in sub-system, system, or vehicle level models. In these instances, an appropriate single finite element representation of a joint could provide adequate representation of a joint's behavior in the structure being modeled. Such a joint element was suggested in Gustafson and Waas,[3] and referred to as a Macroscopic Bonded Joint Finite Element (MBJFE). In concept, it was shown to provide basic joint performance analysis using a very limited number of degrees of freedom. The element's shape functions had a thermo-mechanical, orthotropic, lap-shear type analytical solution embedded within them. The internal displacement (strain) field of the element provided an adequate approximation of the field in a joint. Therefore, it predicted the stress response without significant meshing overhead. The MBJFE was intended to lay a foundation for advances in application specific joint elements for initial sizing in FE models at all system levels.

The work presented in this article is an extension of the work reported previously in Gustafson and Waas,[3] where the embedded solution has an improved stress field over that provided by the analysis in Gustafson et al.[1,2] The virtual work solution presented in Ref. (2) was primarily intended to provide dimensionless parameters and a governing equation which could be used for quick and directionally correct joint design guidance. It did not provide a precise analytical solution for the stress field in the joint. Subsequently, the MBJFE provided in Ref. (3) was a proof-of-concept element which could allow a finite element analyst to represent a structural joint with a single element, while adequately predicting the stress field inside that joint. Since that element was based on a solution which was not precise, the inclusion of a more accurate solution into the MBJFE is desirable. This article intends to provide a solution that has improved accuracy over its predecessor, and to report its inclusion within a MBJFE.

It would be a redundant and lengthy endeavor to include a complete mathematical derivation of the virtual work solution of the governing stress equation presented in this article.[b] The form of the equation used in this work, as well as its solution, were provided in Refs. ([1,2]). Similarly, the formulation of the finite element (reported in Ref. (3)) does not need to be rederived, since only the stress equations and shape functions must be updated to improve its accuracy. As a result, this article will be written with frequent reference to the prior work. For brevity, most of the equations which would be identical (if repeated) are referenced and omitted from this article. Similarly, there are comparatively few references to other double lap analytical solutions, since Ref. (2) contains a summary of the current literature.

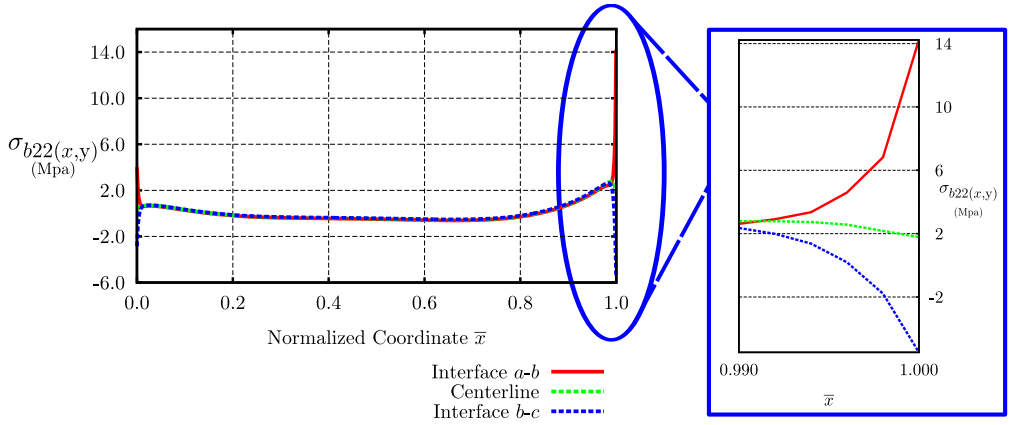

Figure 1: Typical peel stress distribution doe to mixed loading

In considering the solution accuracy required for the proposed MBJFE technique, it is well recognized that there are many factors which effect the stress field and associated joint failure. These include adhesive spew[7] or the geometric discontinuity and unbound stresses associated with stepwise geometries.[34] Additionally, material non-linearity has a significant effect on the stress field,[35,36] which requires a level of material characterization that is often not available early in an analysis cycle. All of the specialized joint analysis techniques (cohesive elements, the virtual crack closure technique, as well as others) require high level and additional material properties. In many circumstances, a designer has insufficient information or time to obtain a *highly accurate* solution, and instead would prefer a simple, directionally correct analysis. These

[b]The authors intend to present a complete derivation of all aspects of the MBJFE in an upcoming journal submission[33].

types of analyses are often useful in tradeoff studies and to identify likely problem areas needing further study.

With that goal in mind, it might be considered adequate to perform linear elastic FE analysis with a basic geometry (*ie* square corners), similar to the continuum FE analysis used for comparison in this article. However, in such a solution, the singular stress field causes a broad range of predicted stresses near the edges, particularly at the material interfaces. For example, a typical result for predicted $\sigma_{b22}(x, y)$ is highlighted in figure 1.

It is apparent that the peel stress can be determined as a function of longitudinal position over most of the joint. However, in the critical areas near the edges of the joint, the predicted stress field varies widely and is mesh dependent. The severity of the mesh dependency is shown in figure 2, where the predicted stress increases without bound with increasing element density. Even when non-linear material properties are assumed, which sometimes can ensure that the stress remains bounded,[35] mesh dependency and convergence remains a concern. It is common practice that an analyst create several meshes at different densities in order to verify that the stress results have converged. The work presented by Smeltzer and Lundgren[31] is a recent example of this practice.

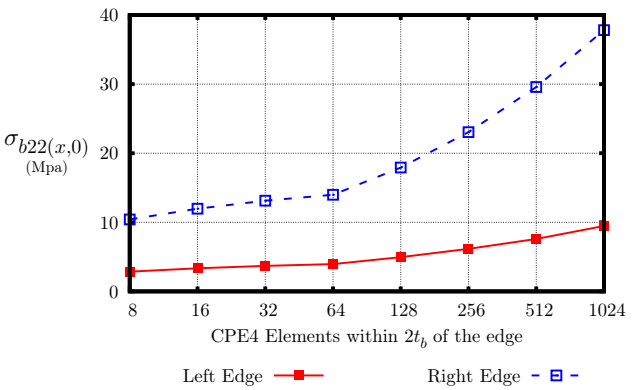

Figure 2: In a linear elastic analysis with stepwise geometry, the mesh does not converge.

In light of the alternatives presented above and in order to be useful to an analyst, the proposed MBJFE must accurately represent the magnitude of the most critical stresses in the joint, while consistently and correctly predicting the trends from joint-to-joint. It must also do this with no mesh dependency and very little meshing overhead. Further, its use must not directly burden the user with the significant calculations typically associated with analytical solutions. In the remaining sections of this article, a macroscopic joint element is presented and is shown to meet these requirements.

II. Derivation of the advanced shear and peel model

In Gustafson et al.,[2] a dimensionless solution was presented for a symmetric, orthotropic double lap joint subjected to thermo-mechanical loading. The lap joint is schematically represented in figure 3. The central adherend is referred to as material a, the outer adherend is referred to as material c. Material b is the adhesive, which is thin in comparison to the adherends. The objective is to determine the equilibrium stress response to thermal and mechanical loading. The material is assumed to be linear elastic and orthotropic, with linear orthotropic thermal expansion. The joint is assumed to deform in plane strain, where the material constitutive response is given by Eq. (21) in appendix V.

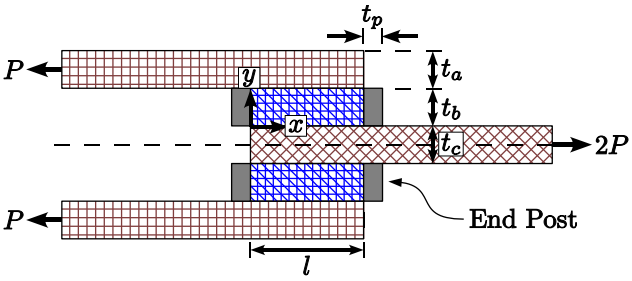

Figure 3: Schematic of the double lap joint with end posts

Examining a general parallelepiped as shown in figure 4, force equilibrium in x and y directions can be written as:

$$\begin{aligned} \sum F_1 &= \delta y\left(\sigma_{11}(x+\delta x, y) - \sigma_{11}(x, y)\right) + \delta x\left(\tau_{12}(x, y+\delta y) - \tau_{12}(x, y)\right) = 0 \\ \sum F_2 &= \delta x\left(\sigma_{22}(x, y+\delta y) - \sigma_{22}(x, y)\right) + \delta y\left(\tau_{12}(x+\delta x, y) - \tau_{12}(x, y)\right) = 0, \end{aligned} \tag{1}$$

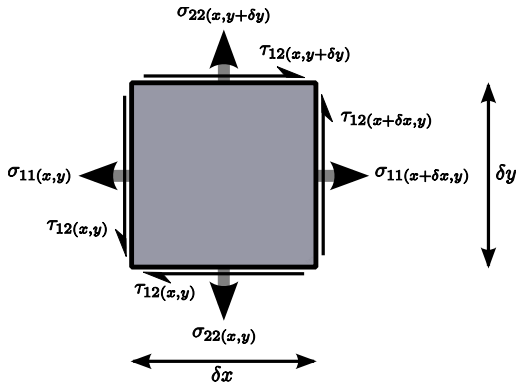

Figure 4: Generalized equilibrium parallelepiped

which can be rewritten as the shear-normal stress relationship for each constituent:

$$\begin{aligned} \frac{\partial \sigma_{11}(x,y)}{\partial x} &= -\frac{\partial \tau_{12}(x,y)}{\partial y} \\ \frac{\partial \sigma_{22}(x,y)}{\partial y} &= -\frac{\partial \tau_{12}(x,y)}{\partial x}. \end{aligned} \tag{2}$$

Several additional assumptions are made to ease the solution. The longitudinal normal stress in the adhesive is assumed to be zero, therefore Eqs. (2) dictates that the shear stress in the adhesive is a function of x only.[c] For convenience, the remaining shear stress fields are assumed to vary linearly in y throughout the specimen, therefore Eqs. (2) dictate that the adherend longitudinal normal stresses are also functions of x only, and that the peel stresses are linear functions of x and y.

Traction free boundaries are present on the top and bottom surfaces. The centerline of the central adherend is free of shear due to symmetry. These requirements are expressed as:

$$\begin{aligned} \tau_{c12(x,t_b+t_c)} &= 0, \\ \sigma_{c22(x,t_b+t_c)} &= 0, \\ \tau_{a12(x,-\frac{t_a}{2})} &= 0. \end{aligned} \tag{3}$$

Stress continuity at the joint interfaces requires the following:

$$\begin{aligned} \sigma_{b22(x,0)} &= \sigma_{a22(x,0)}, \\ \sigma_{c22(x,tb)} &= \sigma_{b22(x,tb)}, \\ \tau_{b12(x,0)} &= \tau_{a12(x,0)}, \\ \tau_{c12(x,tb)} &= \tau_{b12(x,tb)}. \end{aligned} \tag{4}$$

Finally, longitudinal normal stress boundary conditions are imposed by the mechanical loads at the edges of central adherend a, and are expressed as:

$$\begin{aligned} \sigma_{a11(0)} &= 0, \\ \sigma_{a11(l)} &= \frac{2P}{t_a}, \end{aligned} \tag{5}$$

By sequentially writing a linear form for each stress component (using the stress field character described above), and by applying boundary and continuity conditions to determine the linear constants, equations can be written for each stress component in terms of the central adherend stress $\sigma_{a11}(x)$. The process is as described in Ref. (2) and is the same in this work, with the addition of several stress components ($\tau_{a12}(x,y)$, $\sigma_{a22}(x,y)$, $\tau_{c12}(x,y)$, $\sigma_{c22}(x,y)$). The resulting stress equations are detailed on the left side of table 1.

[c]The limitations imposed by this assumption are described in Gustafson et al.[2]

Table 1: Double lap joint stresses and virtual stresses expressed as functions of $\sigma_{a11}(x)$

Equilibrium Normal Stress	Virtual Normal Stress
$\sigma_{a11}(x)$	$\hat{\sigma}_{a11}(x)$
$\sigma_{c11}(x) = \frac{P}{t_c} - \frac{t_a\,\sigma_{a11}(x)}{2\,t_c}$	$\hat{\sigma}_{c11}(x,y) = -\frac{t_a\,\hat{\sigma}_{a11}(x)}{2\,t_c}$
$\sigma_{a22}(x,y) = \frac{d^2}{dx^2}\sigma_{a11}(x)\left(\frac{y^2+t_a y}{2} - \frac{t_a(t_c+2t_b)}{4}\right)$	$\hat{\sigma}_{a22}(x,y) = \frac{d^2}{dx^2}\hat{\sigma}_{a11}(x)\left(\frac{y^2+t_a y}{2} - \frac{t_a(t_c+2t_b)}{4}\right)$
$\sigma_{b22}(x,y) = \frac{t_a\left(\frac{d^2}{dx^2}\sigma_{a11}(x)\right)(2y-t_c-2t_b)}{4}$	$\hat{\sigma}_{b22}(x,y) = \frac{t_a\left(\frac{d^2}{dx^2}\hat{\sigma}_{a11}(x)\right)(2y-t_c-2t_b)}{4}$
$\sigma_{c22}(x,y) = -\frac{t_a\left(\frac{d^2}{dx^2}\sigma_{a11}(x)\right)(y-t_c-t_b)^2}{4t_c}$	$\hat{\sigma}_{c22}(x,y) = -\frac{t_a\left(\frac{d^2}{dx^2}\hat{\sigma}_{a11}(x)\right)(y-t_c-t_b)^2}{4t_c}$
Equilibrium Shear Stress	**Virtual Shear Stress**
$\tau_{a12}(x,y) = -\frac{\frac{d}{dx}\sigma_{a11}(x)(2y+t_a)}{2}$	$\hat{\tau}_{a12}(x,y) = -\frac{\frac{d}{dx}\hat{\sigma}_{a11}(x)(2y+t_a)}{2}$
$\tau_{b12}(x) = -\frac{t_a\left(\frac{d}{dx}\sigma_{a11}(x)\right)}{2}$	$\hat{\tau}_{b12}(x,y) = -\frac{t_a\left(\frac{d}{dx}\hat{\sigma}_{a11}(x)\right)}{2}$
$\tau_{c12}(x,y) = \frac{t_a\left(\frac{d}{dx}\sigma_{a11}(x)\right)(y-t_c-t_b)}{2t_c}$	$\hat{\tau}_{c12}(x,y) = \frac{t_a\left(\frac{d}{dx}\hat{\sigma}_{a11}(x)\right)(y-t_c-t_b)}{2t_c}$
Equilibrium End Post Stress	**Virtual End Post Stress**
$\sigma_{p22}(\bar{x}=0,y) = \frac{t_a\left(\frac{d}{d\,x}\,\sigma_{a11}(x)\right)(y-t_b)}{2\,t_p}$	$\hat{\sigma}_{p22}(\bar{x}=0,y) = \frac{t_a\left(\frac{d}{d\,x}\,\hat{\sigma}_{a11}(x)\right)(y-t_b)}{2\,t_p}$
$\sigma_{p22}(\bar{x}=1,y) = -\frac{t_a\left(\frac{d}{d\,x}\,\sigma_{a11}(x)\right)(y-t_b)}{2\,t_p}$	$\hat{\sigma}_{p22}(\bar{x}=1,y) = -\frac{t_a\left(\frac{d}{d\,x}\,\hat{\sigma}_{a11}(x)\right)(y-t_b)}{2\,t_p}$

In addition to the boundary conditions specified in Eqs. (3), Eqs. (4), and Eqs. (5), the adhesive edge shear stress is forced to zero using the end post technique described in Gustafson et al.,[2] which was inspired by the double lap joint solution of Davies.[37] The stresses in the edge posts also listed on the left side of table 1.

The solution for the central adherend normal stress ($\sigma_{a11}(x)$) is carried out by application of the principle of virtual forces, as described in detail in appendix V. In summary, for each stress component (each is a function of $\sigma_{a11}(x)$), a corresponding virtual stress component is written in terms of the virtual normal stress $\hat{\sigma}_{a11}(x)$. These virtual stress components are shown on the right side of table 1. By integrating potential energy over the volume of the joint and minimizing for any admissible $\hat{\sigma}_{a11}(x)$, the central adherend stress field $\sigma_{a11}(x)$ is determined as a function of all material properties and loads. Subsequent grouping of all material terms according to their order of derivative (defined as β and γ in Eq. (6)) and the loads according to thermal and mechanical contributions of the total load (defined as ϕ_T and ϕ_P respectively in Eq. (6)), the differential equation can be written as:

$$\frac{\partial^4\sigma_{a11}(x)}{\partial x^4} + \beta\frac{\partial^2\sigma_{a11}(x)}{\partial x^2} + \gamma\sigma_{a11}(x) + \phi_T + \phi_P = 0. \tag{6}$$

Eq. (6) is identical in form to the solution given in,[2] however the material constants β and γ, as well as the load constants ϕ_T and ϕ_P are more complex due to the increase in the retained stress components in the potential energy minimization. The improved accuracy of this model over its predecessor is a direct result of the addition of these previously neglected terms.

With an equation for the central adherend stress ($\sigma_{a11}(x)$), all stress components can easily be determined using the equations in table 1. It was noted in Ref. (2) that non-dimensionalization and load normalization of (6) is possible, and doing so provides a mechanism for separation of the responses to mechanical and thermal loads. As described in Ref. (3), this has great benefits for the MBJFE solution when used with an iterative solver. Therefore, without explicitly reporting the dimensional material and load constants (β, γ, ϕ_T, ϕ_P), non-dimensionalization and load normalization is done so as to conform to the solution provided

in Ref. (2). The dimensionless and load normalized material, load, and stress terms are defined as follows:

$$\begin{aligned}
\bar{x} &= \frac{x}{l}, \\
\bar{\beta} &= l^2\beta, \\
\bar{\gamma} &= l^4\gamma, \\
\bar{\phi}_T &= \phi_T \frac{l^4}{E_{a11}}, \\
\bar{\phi}_P &= \phi_P \frac{l^4}{E_{a11}}, \\
\bar{\bar{\phi}}_{total} &= \bar{\phi}_P + \bar{\phi}_T, \\
\bar{\bar{\phi}}_P &= \frac{\bar{\phi}_P}{\bar{\bar{\phi}}_{total}}, \\
\bar{\bar{\sigma}}_{\kappa ij(\bar{x})} &= \frac{\sigma_{\kappa ij(l\bar{x})}}{E_{a11}\bar{\bar{\phi}}_{total}}.
\end{aligned} \tag{7}$$

In Eq. (7), $\bar{x}$ is the dimensionless spatial coordinate measured from the left edge of the joint, $\bar{\beta}$ and $\bar{\gamma}$ are dimensionless material parameters, and $\bar{\phi}_P$ and $\bar{\phi}_T$ are the dimensionless mechanical and thermal loads respectively. A dimensionless total load is defined as $\bar{\bar{\phi}}_{total}$, which is used to further normalize the stresses $\bar{\bar{\sigma}}_{\kappa ij(\bar{x})}$. Similarly, a mechanical fraction of the dimensionless total load is defined as $\bar{\bar{\phi}}_P$. Each of the terms in Eq. (7) are explicitly defined according to the constitutive and load quantities in appendix V. Now, Eq. (8) from Ref. (2) is written as the form most suitable for the MBJFE:

$$\bar{\bar{\sigma}}_{a11}\left(\bar{x}, \bar{\bar{\phi}}_P\right) = \bar{\bar{A}}\left(\bar{\bar{\phi}}_P\right) e^{\bar{\lambda}_1\bar{x}} + \bar{\bar{B}}\left(\bar{\bar{\phi}}_P\right) e^{-\bar{\lambda}_1\bar{x}} + \bar{\bar{C}}\left(\bar{\bar{\phi}}_P\right) e^{\bar{\lambda}_3\bar{x}} + \bar{\bar{D}}\left(\bar{\bar{\phi}}_P\right) e^{-\bar{\lambda}_3\bar{x}} - \frac{1}{\gamma}. \tag{8}$$

In Eq. (8), the material parameters[d] are recast in the form of the roots of the bi-quadratic differential equation.

$$\bar{\lambda}^2_{[12]} = \frac{-\bar{\beta} \pm \sqrt{\bar{\beta}^2 - 4\bar{\gamma}}}{2}. \tag{9}$$

The equations for the dimensionless basis coefficients ($\bar{\bar{A}}\left(\bar{\bar{\phi}}_P\right)$, $\bar{\bar{B}}\left(\bar{\bar{\phi}}_P\right)$, $\bar{\bar{C}}\left(\bar{\bar{\phi}}_P\right)$, $\bar{\bar{D}}\left(\bar{\bar{\phi}}_P\right)$) are identical to those given in Ref. (2) and are listed below:

$$\begin{aligned}
\bar{\bar{A}}\left(\bar{\bar{\phi}}_P\right) &= \frac{\mu_3\mu_{A_P}}{\mu_1\mu_2}\bar{\bar{\phi}}_P + \frac{\mu_{A_T}}{\mu_1}, \\
\bar{\bar{B}}\left(\bar{\bar{\phi}}_P\right) &= \frac{\mu_3\mu_{B_P}}{\mu_1\mu_2}\bar{\bar{\phi}}_P + \frac{\mu_{B_T}}{\mu_1}, \\
\bar{\bar{C}}\left(\bar{\bar{\phi}}_P\right) &= \frac{\mu_3\mu_{C_P}}{\mu_1\mu_2}\bar{\bar{\phi}}_P + \frac{\mu_{C_T}}{\mu_1}, \\
\bar{\bar{D}}\left(\bar{\bar{\phi}}_P\right) &= \frac{\mu_3\mu_{D_P}}{\mu_1\mu_2}\bar{\bar{\phi}}_P + \frac{\mu_{D_T}}{\mu_1},
\end{aligned} \tag{10}$$

In Eq. (10), the coefficients ($\bar{\bar{A}}\left(\bar{\bar{\phi}}_P\right)$, $\bar{\bar{B}}\left(\bar{\bar{\phi}}_P\right)$, $\bar{\bar{C}}\left(\bar{\bar{\phi}}_P\right)$, $\bar{\bar{D}}\left(\bar{\bar{\phi}}_P\right)$) are linear functions of the mechanical fraction of the total load ($\bar{\bar{\phi}}_P$) and several variables denoted by μ which are combinations of the material parameters. These are listed in the appendix F. In combination, Eq. (8) and Eq. (10) effectively separate the thermal and mechanical responses.

It is recognized that the presented solution in this section would be incomplete without additional information provided in Ref. (2), particularly with respect to the application of boundary conditions which bridge between the differential equation (Eq. (6)) and the stress solution (Eq. (8)). Further, Ref. (2) provides complete detail regarding the load normalized form of Eq. (8).

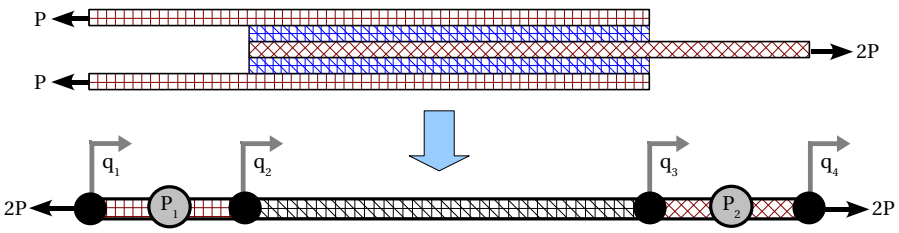

Figure 5: Symmetric double lap joint and MBJFE representation.

III. Formulation of the finite element

Figure 5 schematically shows the MBJFE originally derived in Gustafson and Waas.[3] The element is a 1D element, with all displacement degrees of freedom being oriented along the 1-axis. Two of the displacement degrees of freedom, q_1 and q_4, are external degrees of freedom which connect the joint element to the external structure. The remaining displacement degrees of freedom are internal to the element, and are used in conjunction with Lagrange multipliers to determine the mechanical loading fraction, $\bar{\bar{\phi}}_P$, required for determination of the stress and strain fields governed by Eq. (8). The mechanical load that is carried across the joint is calculated using internal degrees of freedom, P_1 and P_2 .

The element in figure 5 is composed of three subelements. The outer subelements span q_1 - q_2, and q_3 - q_4. These subelements are essentially truss elements, and their principal purpose is to establish the mechanical load as an internal degree of freedom as described in Ref. (3), where their contribution to the element stiffness is given in detail. The joint section subelement spans q_2 - q_3, and is responsible for predicting the relevant joint stresses as well as correctly representing the stiffness of the joint. The form of the stiffness matrix was developed in Ref. (3). To update the subelement to the more accurate stress functions developed above, the displacement interpolation (shape functions) must be updated, as is detailed in subsection A.

A. Stiffness and Load Contribution of the Adhesively Bonded Section

The subelement stiffness matrix is directly dependent on the load-displacement response of the central and outer adherends. The strain in these adherends is related, via the material constitutive response given in Eq. (21), to the stress fields known from Eq. (8) and table 1. These strains are related to the stiffness matrix by shape functions derivatives, and this relationship was given in Ref. (3) as Eq. (11).

$$K_e = \frac{\sum_{\kappa} E_{\kappa 11} \int_{y_{\kappa 0}}^{y_{\kappa 1}} \int_0^1 B_\kappa^2 \left(\bar{x}, \bar{\bar{\phi}}_P\right) d\bar{x}\, dy_\kappa}{l_e} \begin{bmatrix} 1 & -1 \\ -1 & 1 \end{bmatrix} \tag{11}$$

In the discrete space of the FE model, the known or desired quantities are the applied temperature change (ΔT, assumed to be constant through the element) and the nodal loads and displacements. The load quantities must be recast into their non-dimensional forms to conform to the stress equations given above. Non-dimensionalizing constants ($\frac{\Theta}{\theta_{\Delta T}}$ and $\frac{\Theta}{\theta_P}$) are defined so that:

$$\begin{aligned} \Delta T &= \frac{\Theta}{\theta_{\Delta T}} \bar{\phi}_T, \\ P &= \frac{\Theta}{\theta_P} \bar{\phi}_P. \end{aligned} \tag{12}$$

[d] In Ref. (1) the roots of the bi-quadratic equation were listed as $\bar{\lambda}_{[12]}$, whereas Refs. ([2,3]) had them listed as $\bar{\lambda}_{[13]}$. The latter is chosen for this article in an attempt to maintain consistency with the more recent work.

Application of Eqs. (12) to the known stress field and constitutive law, the strain can be written as a linear function of the total load $\bar{\bar{\phi}}_{total}$:

$$\begin{aligned}
\frac{\varepsilon_{a11}\left(\bar{x},\bar{\bar{\phi}}_P,\bar{\bar{\phi}}_{total}\right)}{\bar{\bar{\phi}}_{total}} =& (1-\nu_{a13}\nu_{a31})\left(e^{-\bar{\lambda}_3\bar{x}}\bar{\bar{D}}\left(\bar{\bar{\phi}}_P\right)+e^{\bar{\lambda}_3\bar{x}}\bar{\bar{C}}\left(\bar{\bar{\phi}}_P\right)+e^{-\bar{\lambda}_1\bar{x}}\bar{\bar{B}}\left(\bar{\bar{\phi}}_P\right)+e^{\bar{\lambda}_1\bar{x}}\bar{\bar{A}}\left(\bar{\bar{\phi}}_P\right)-\frac{1}{\bar{\gamma}}\right)\\
&+\frac{\Theta}{\theta_{\Delta T}}\left(1-\bar{\bar{\phi}}_P\right)\left(\alpha_{a33}\nu_{a31}+\alpha_{a11}\right),\\
\frac{\varepsilon_{c11}\left(\bar{x},\bar{\bar{\phi}}_P,\bar{\bar{\phi}}_{total}\right)}{\bar{\bar{\phi}}_{total}} =& \frac{E_{a11}t_a\left(\nu_{c13}\nu_{c31}-1\right)}{2E_{c11}t_c}\left(e^{-\bar{\lambda}_3\bar{x}}\bar{\bar{D}}\left(\bar{\bar{\phi}}_P\right)+e^{\bar{\lambda}_3\bar{x}}\bar{\bar{C}}\left(\bar{\bar{\phi}}_P\right)+e^{-\bar{\lambda}_1\bar{x}}\bar{\bar{B}}\left(\bar{\bar{\phi}}_P\right)+e^{\bar{\lambda}_1\bar{x}}\bar{\bar{A}}\left(\bar{\bar{\phi}}_P\right)\right)\\
&+\frac{\Theta}{\theta_{\Delta T}}\left(1-\bar{\bar{\phi}}_P\right)\left(\alpha_{c11}+\alpha_{c33}\nu_{c31}\right)\\
&+\frac{1}{E_{c11}t_c}\left(1-\nu_{c13}\nu_{c31}\right)\left(\frac{E_{a11}t_a}{2\bar{\gamma}}+\frac{\bar{\bar{\phi}}_P\frac{\Theta}{\theta_P}}{1}\right).
\end{aligned} \tag{13}$$

It is assumed that the total elongation is the same for the adherends, therefore the two elongation equations are written as:

$$\begin{aligned}
q_e &= \left(\frac{dx}{d\bar{x}}\right)\int_0^1 \varepsilon_{a11}\left(\bar{x},\bar{\bar{\phi}}_P,\bar{\bar{\phi}}_{total}\right)d\bar{x},\\
q_e &= \left(\frac{dx}{d\bar{x}}\right)\int_0^1 \varepsilon_{c11}\left(\bar{x},y,\bar{\bar{\phi}}_P,\bar{\bar{\phi}}_{total}\right)d\bar{x},
\end{aligned} \tag{14}$$

where the subelement elongation q_e is defined as:

$$q_e = q_4 - q_3. \tag{15}$$

In Eq. (14), the elongation is written as a function of the non-dimensional total load, $\bar{\bar{\phi}}_{total}$. The total load is not known *a priori* and must be eliminated in favor of an available quantity (the total elongation q_e) so that a stiffness matrix can be calculated. This is accomplished by applying the boundary condition to the result of Eq. (14):

$$\begin{aligned}
\left(\frac{dx}{d\bar{x}}\right)\int_0^{\bar{x}} \varepsilon_{a11}\left(\bar{x},\bar{\bar{\phi}}_P,\bar{\bar{\phi}}_{total}\right)d\bar{x}\Big|_{\bar{x}=0} &= 0,\\
\left(\frac{dx}{d\bar{x}}\right)\int_0^{\bar{x}} \varepsilon_{a11}\left(\bar{x},\bar{\bar{\phi}}_P,\bar{\bar{\phi}}_{total}\right)d\bar{x}\Big|_{\bar{x}=1} &= q_e,\\
\left(\frac{dx}{d\bar{x}}\right)\int_0^{\bar{x}} \varepsilon_{c11}\left(\bar{x},\bar{\bar{\phi}}_P,\bar{\bar{\phi}}_{total}\right)d\bar{x}\Big|_{\bar{x}=0} &= 0,\\
\left(\frac{dx}{d\bar{x}}\right)\int_0^{\bar{x}} \varepsilon_{c11}\left(\bar{x},\bar{\bar{\phi}}_P,\bar{\bar{\phi}}_{total}\right)d\bar{x}\Big|_{\bar{x}=1} &= q_e,
\end{aligned} \tag{16}$$

Specifically, the elongation is zero when $\bar{x}=0$ (since $\bar{x}=0$ is the reference from which elongation is measured), and the total elongation is q_e when $\bar{x}=1$. Applying these boundary conditions and solving for the total load $\bar{\bar{\phi}}_{total}$ as a function of elongation q_e (this is done for each strain equation), total load can be replaced in Eq. (13) with the following:

$$\begin{aligned}
\bar{\bar{\phi}}_{total_a} &= \bar{\bar{\Phi}}_a q_e,\\
\bar{\bar{\phi}}_{total_c} &= \bar{\bar{\Phi}}_c q_e,
\end{aligned} \tag{17}$$

where the constants ($\bar{\bar{\Phi}}_a$, $\bar{\bar{\Phi}}_c$) are detailed in appendix E. Substituting Eq. (17) into Eq. (13), the displacement field is known in terms of total elongation and the shape functions and shape functions derivatives can now

be written for each adherend:

$$\begin{aligned} u_a\left(\bar{x},\bar{\bar{\phi}}_P,q_e\right) &= N_a\left(\bar{x},\bar{\bar{\phi}}_P\right)q_e, \\ u_c\left(\bar{x},\bar{\bar{\phi}}_P,q_e\right) &= N_c\left(\bar{x},\bar{\bar{\phi}}_P\right)q_e, \\ B_a\left(\bar{x},\bar{\bar{\phi}}_P\right) &= \frac{d}{d\bar{x}}N_a\left(\bar{x},\bar{\bar{\phi}}_P\right), \\ B_c\left(\bar{x},\bar{\bar{\phi}}_P\right) &= \frac{d}{d\bar{x}}N_c\left(\bar{x},\bar{\bar{\phi}}_P\right). \end{aligned} \tag{18}$$

The complete shape functions in Eq. (18) are detailed in the appendix V.

Having established the appropriate shape functions, the stiffness matrix can now be integrated numerically using Eqs. (11). Additionally, the subelement load vector was derived in Ref. (3) as Eq. (19), and can now be calculated. In Eqs. (11) and Eq. (19), the summation includes both adherends ($\kappa = a, c$).

$$\vec{F} = P\left\{\begin{array}{c} -1 \\ 1 \end{array}\right\} + \sum_{\kappa}\alpha_{\kappa 11}E_{\kappa 11}\left(\int_{y_0}^{y_1}\int_0^1 B_\kappa\left(\bar{x},\bar{\bar{\phi}}_P\right)d\bar{x}\,dy_\kappa\right)\Delta T\left\{\begin{array}{c} -1 \\ 1 \end{array}\right\} \tag{19}$$

The final requirement for element calculations is knowledge of the mechanical load P, used to determine the load character $\bar{\bar{\phi}}_P$ of the bonded section sub-element. This is accomplished by causing this load to be an internal degree of freedom using Lagrange multipliers. In this work, the load becomes P_1.[e] The complete description of this process is as presented in Ref. (1) and is not repeated here.

B. The Abaqus® Subroutine

The sub-element stiffness matrices and load vectors, developed above and in Ref. (3), are assembled into element matrices with 6 DOFs using a standard assembly technique.[38] The formulation requires an iterative solution, since the mechanical load carried by the joint is not known in general. Therefore, the shape functions developed above have been implemented as a user element subroutine (UEL) for the commercial non-linear FE package Abaqus®.[27] A complete description of the UEL functionality is provided in Ref. (3), including the modified midpoint rule numerical integration technique.

Table 2: Model size for ASTM double lap joints

Model	Nodes	Elements	DOFs
CPE4	~ 22100	~ 21600	~ 44300
UEL	4	1	6

The field quantities are calculated from table 1 at each integration point, based on the calculated ΔT and P_1 for the increment. The user specifies the number of integration points to be the number of stress prediction points desired in the joint. In this way, all stress and strain quantities of interest are calculated in a manner consistent with the shape function displacement field.

IV. FE output

The stress prediction provided by the UEL has been compared to a plane strain continuum FE model. In the case of the UEL, the entire model consists of a single element. In the case of the continuum model, a 2D mesh has been generated. Both models are based on the ASTM International double lap joint.[39] An overview of the continuum mesh is shown in figure 6, and the assumed geometries are given in table 3(a). The solver used is Abaqus® Standard, and the continuum mesh consists entirely of linear plain strain elements (CPE4). Half of the joint is modeled due to symmetry. Loading is specified as listed in table 3(b), where the mechanical load is applied far away from the lap joint and the thermal load is applied to all nodes. Displacement symmetry constraints are enforced along the mid-plane of the central adherend. Non-linear geometric stiffness is assumed.

[e]The currently reported formulation of the element carries two internal load degrees of freedom, P_1 and P_2 as shown in figure 5. Strictly speaking, this only requires, and would be most efficiently accomplished using only one additional degree of freedom.

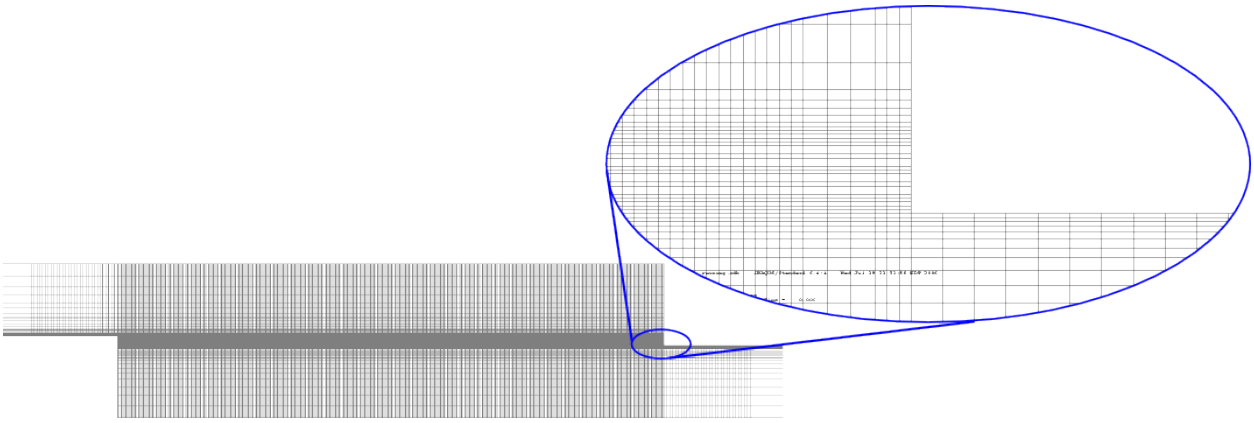

Figure 6: The FE mesh

Aluminum (Al) is used as the central adherend in all models; the outer adherends are Titanium (Ti), and AS4/3501-6 (AS4).[40] For simplicity, the adhesive properties are assumed to be isotropic, and are estimated base on Cytec FM300 adhesive. The assumed material properties are summarized in table 4. The shear stresses from the continuum model are reported at the centerline of the adhesive, which is the most representative location for comparison with the uniform shear stress predicted by the UEL. The peel stress in the continuum model is reported at the interface between the adhesive and the central adherend. The choice of this location has a large effect on the predicted peel stress, as was shown in figure 1. The adhesive to central adherend interface (*a*-*b*) comparison location is chosen because the UEL model can be used as a measure of the *magnitude* of the singularity present at this location. The peel stress reported from the UEL is the average peel stress through the thickness (the stress equation is evaluated at $y = \frac{t_b}{2}$).

Table 3: Geometric and loading assumptions for model comparison

(a) ASTM double lap joint geometric features (mm).

Component	Thickness	Length
Outer Adherend	1.6	76.2
Adhesive	0.2	12.7
Central Adherend	3.2	76.2

(b) Assumed loading.

Load Type	Value
P (N·mm^{-1})	10
ΔT (°C)	10

A. Comparison of MBJFE and continuum based FE models

Plots of the stresses predicted by the continuum and UEL models are shown in figures 7-10. figure 7 shows the predictions for a Al-Al double lap joint. When this joint is subjected to thermal loading, as is shown in 7.1 and 7.2, both models predict that the stress is negligible.[f] This stress result is intuitive, since the two adherends have identical thermal expansion coefficients. Figures 7.3 and 7.4 show shear and peel stress predictions of the Al-Al joint subjected to mechanical loading, where good agreement is found in both figures. The peak shear stress predicted by the UEL is similar to that predicted by the continuum model, though there is a difference in predicted peak location. The peel stress predicted by the UEL is in adequate agreement with the continuum model, and its value does not suffer from any mesh dependency. Figures 7.5 and 7.6 show mixed loading for the Al-Al joint, which is almost identical to the mechanical load predictions for this joint.

Figure 8 shows the stresses predicted by the continuum and UEL models for an Al-Ti joint. Thermal loading is no longer trivial, and the stress predictions resulting from it are shown in 8.1 and 8.2 for shear and peel respectively. In this joint type, the predicted shear stress is in good agreement for thermal, mechanical,

[f]This is a special case of identical adherends which was noted in Ref. (2). Thermal expansion of the adhesive is the *primary* source of loading. Consequently, the longitudinal stress of the adhesive *could* be of primary interest to the analyst. Therefore, an analysis methodology which takes this into account might be chosen.

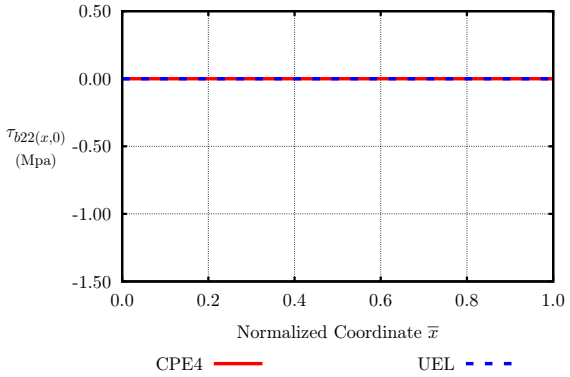

7.1: $\tau_{b12}(x)$ due to $\bar{\phi}_T$

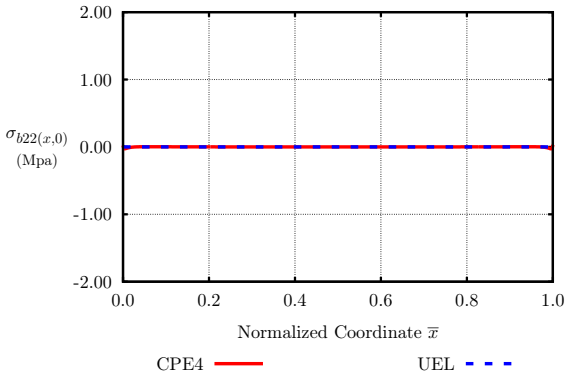

7.2: $\sigma_{b22}(x,y)$ due to $\bar{\phi}_T$

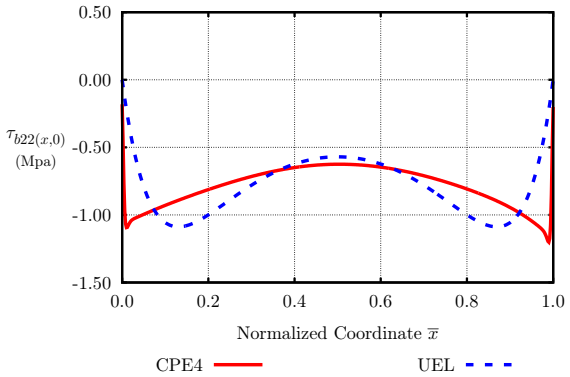

7.3: $\tau_{b12}(x)$ due to $\bar{\phi}_P$

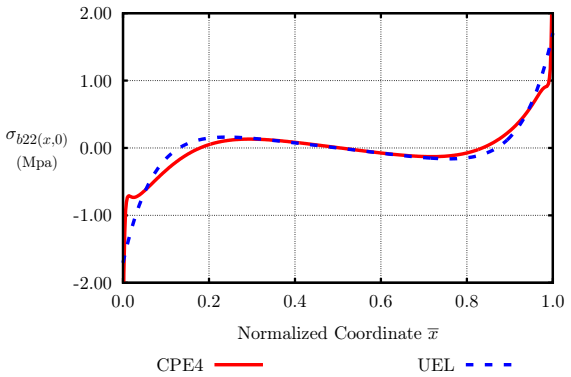

7.4: $\sigma_{b22}(x,y)$ due to $\bar{\phi}_P$

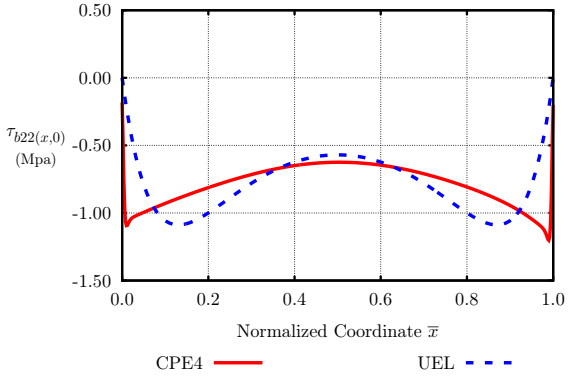

7.5: $\tau_{b12}(x)$ due to $\bar{\phi}_P + \bar{\phi}_T$

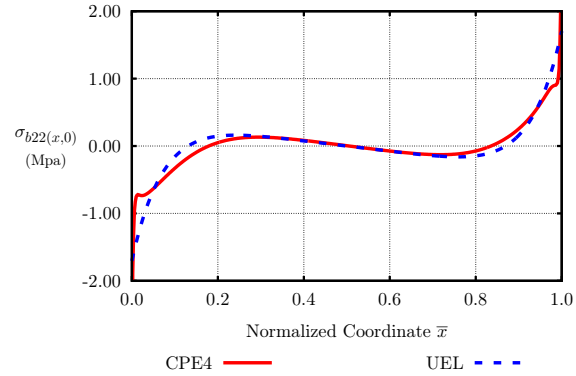

7.6: $\sigma_{b22}(x,y)$ due to $\bar{\phi}_P + \bar{\phi}_T$

Figure 7: Continuum and UEL models of Al-Al joint

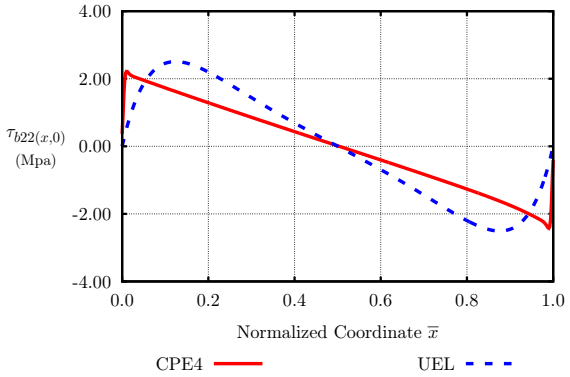

8.1: $\tau_{b12}(x)$ due to $\bar{\phi}_T$

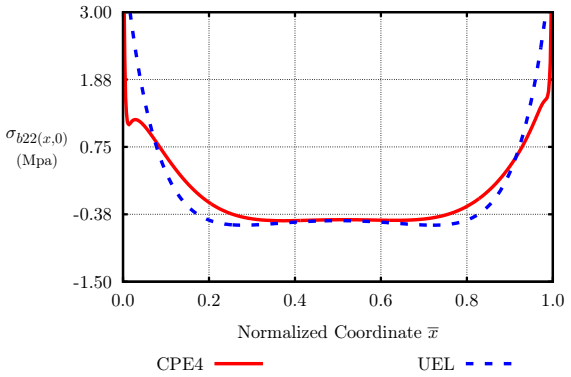

8.2: $\sigma_{b22}(x,y)$ due to $\bar{\phi}_T$

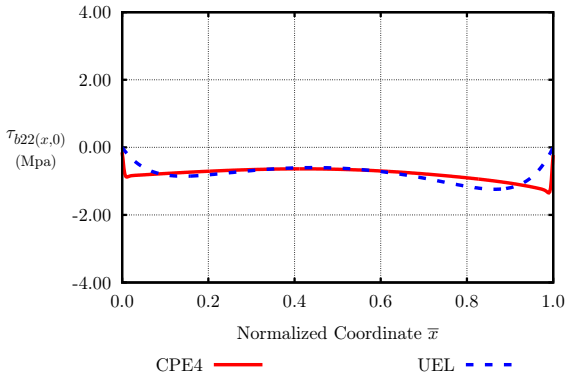

8.3: $\tau_{b12}(x)$ due to $\bar{\phi}_P$

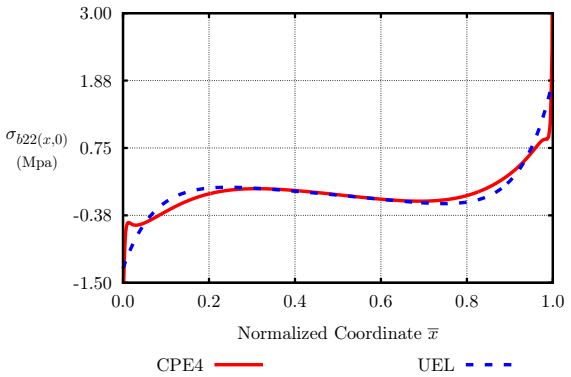

8.4: $\sigma_{b22}(x,y)$ due to $\bar{\phi}_P$

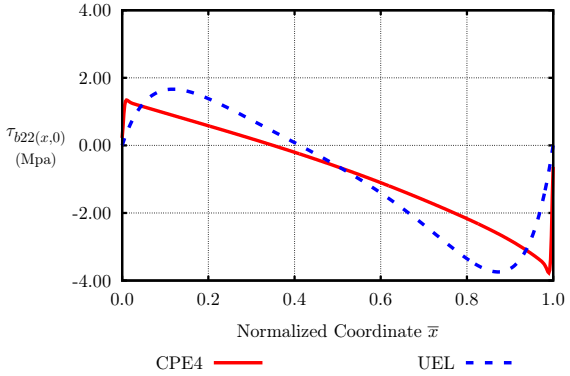

8.5: $\tau_{b12}(x)$ due to $\bar{\phi}_P + \bar{\phi}_T$

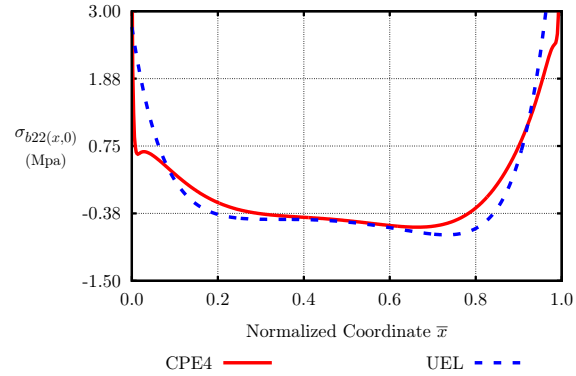

8.6: $\sigma_{b22}(x,y)$ due to $\bar{\phi}_P + \bar{\phi}_T$

Figure 8: Continuum and UEL models of Al-Ti joint

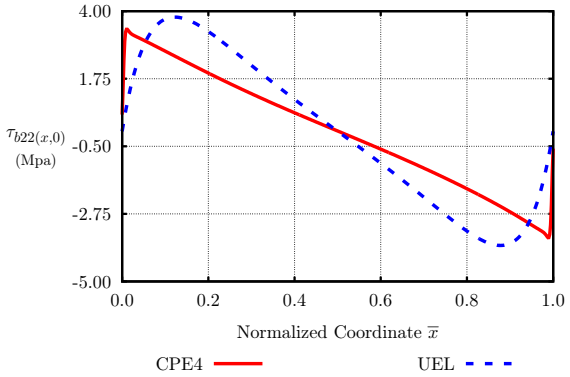

9.1: $\tau_{b12}(x)$ due to $\bar{\phi}_T$

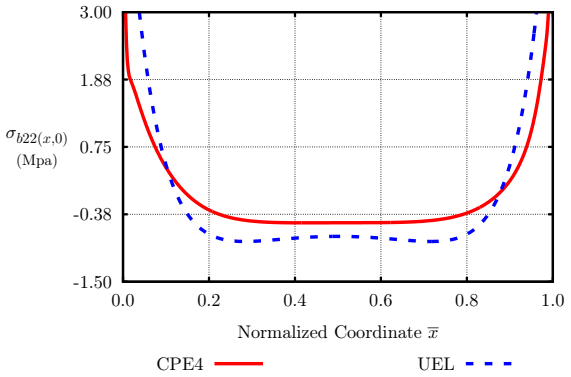

9.2: $\sigma_{b22}(x, y)$ due to $\bar{\phi}_T$

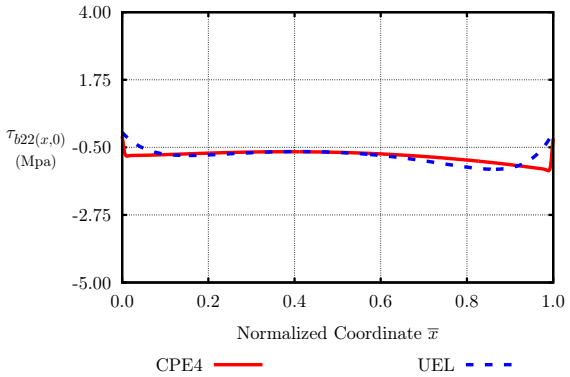

9.3: $\tau_{b12}(x)$ due to $\bar{\phi}_P$

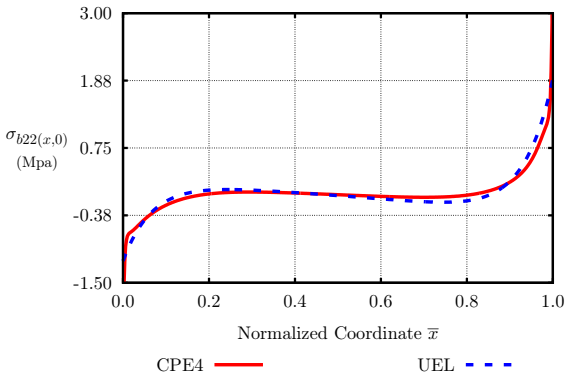

9.4: $\sigma_{b22}(x, y)$ due to $\bar{\phi}_P$

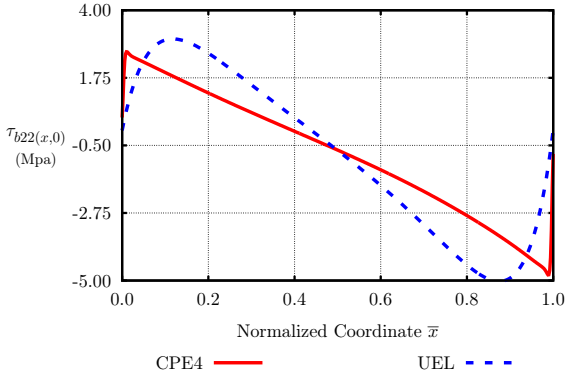

9.5: $\tau_{b12}(x)$ due to $\bar{\phi}_P + \bar{\phi}_T$

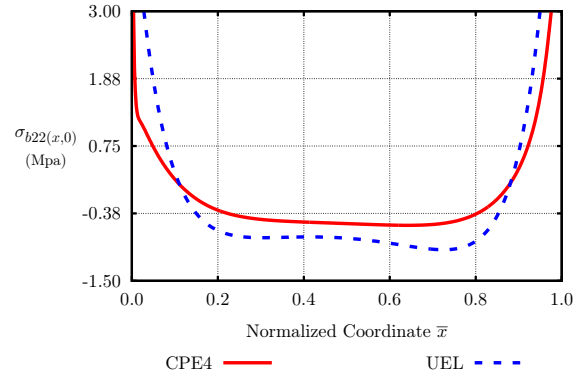

9.6: $\sigma_{b22}(x, y)$ due to $\bar{\phi}_P + \bar{\phi}_T$

Figure 9: Continuum and UEL models of Al-AS4 (0°) joint

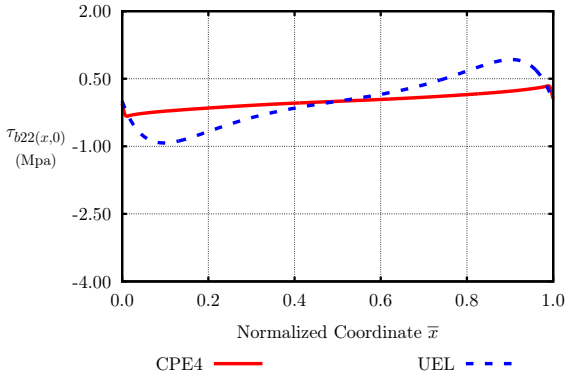

10.1: $\tau_{b12}(x)$ due to $\bar{\phi}_T$

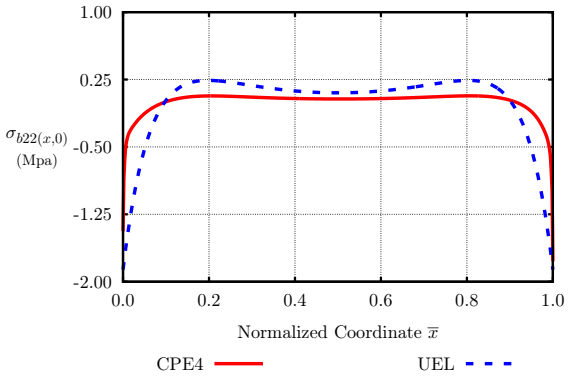

10.2: $\sigma_{b22}(x, y)$ due to $\bar{\phi}_T$

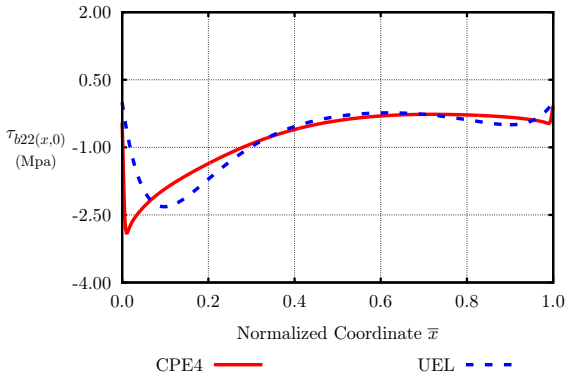

10.3: $\tau_{b12}(x)$ due to $\bar{\phi}_P$

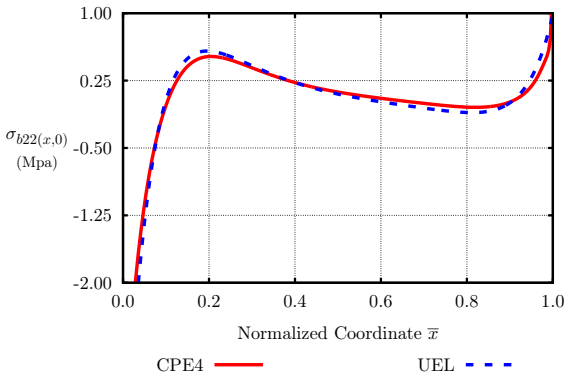

10.4: $\sigma_{b22}(x, y)$ due to $\bar{\phi}_P$

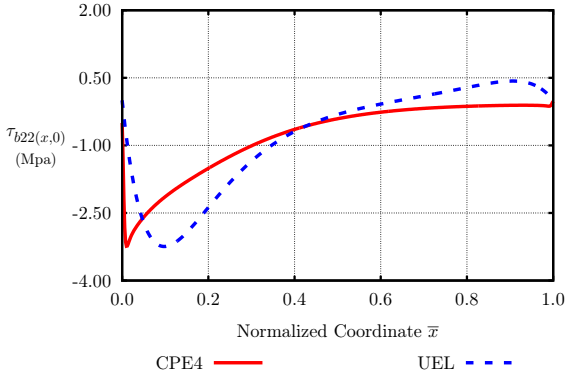

10.5: $\tau_{b12}(x)$ due to $\bar{\phi}_P + \bar{\phi}_T$

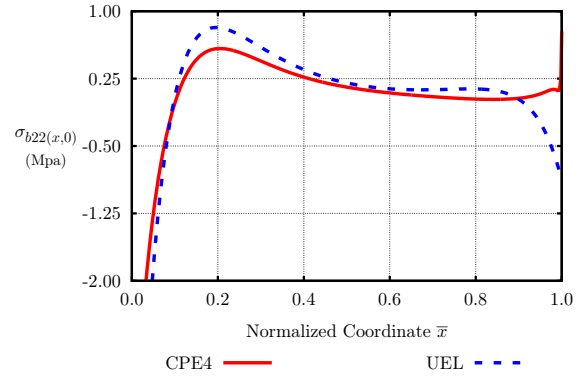

10.6: $\sigma_{b22}(x, y)$ due to $\bar{\phi}_P + \bar{\phi}_T$

Figure 10: Continuum and UEL models of Al-AS4 (90°) joint

and mixed loading, as is shown in 8.1, 8.3 and 8.5. In all cases, the peak shear stress predicted by the UEL matches the continuum model adequately, and the peak location is consistently found to be further from the edge in the UEL than in the continuum model. Looking at the peel stress predictions shown in 8.2, 8.4 and 8.6, good agreement is found again. The stress predicted by the UEL is similar to the continuum model, and is representative of the unconverged singular peel stress result.

The UEL solution is orthotropic, and an example of a composite application is shown in figures 9 and 10. The figures show two Al-AS4 joints subjected to thermal, mechanical, and mixed loading. The laminate shown in figure 9 has fibers oriented longitudinally (0^o), and the laminate shown in figure 10 has fibers oriented transversely (90^o). Despite the unlikelihood of the 90^o fiber orientation (relative to the joint loading axis) being used in practical applications, the two figures shows that the UEL solution is in adequate agreement with the continuum solution in both cases and for all three load types.

Based on the cumulative agreement shown in figures 7-10, it can be concluded that the UEL element adequately predicts the shear stress in a double lap joint. The peel stress predicted by the UEL model is found to be consistently in agreement with the *magnitude* of the (unconverged) singular stress field in all figures (at the mesh density used in this comparison). Therefore, it can be used as a mesh independent indicator of peel stress magnitude, useful for joint-to-joint comparison.

V. Conclusion

In this article, a Macroscopic Bonded Joint Finite Element has been described. It is capable of predicting the lap joint field quantities in the bonded zone while using only six degrees of freedom. It does so without burdening the user with mesh dependency or significant meshing overhead. The described MBJFE accomplishes this task by embedding an analytical solution directly within the element. Its stiffness and load response are based on non-linear shape functions that are dependent on the load character. All critical terms are formulated as functions of the dimensionless mechanical load fraction, $\bar{\bar{\phi}}_P$, allowing for solution via an iterative, non-linear FE solver. To demonstrate its capability, the element has been implemented as a user element subroutine in the commercial finite element package Abaqus®.

Based on comparison with a traditional FE solution, the MBJFE has been shown to be capable of adequately predicting stress and strain due to thermal and mechanical loads in a single, four noded element with six degrees of freedom. With this element, initial sizing and trade studies can be accomplished with a greatly reduced meshing investment, as well as a reduction in computation time, when compared with the standard finite element method. This work lays a firm foundation for further advancements in macroscopic joint elements. It is anticipated that currently available analytical solutions can be reformulated as application specific macroscopic joint elements.

Extended description of the virtual work calculations

The principal of virtual work calculations are briefly summarized below. Equilibrium relations derived in section II are given in table 1, as well as their associated virtual stress quantities. In table 1, all virtual stress quantities can be written in terms of the central adherend virtual stress $\hat{\sigma}_{a11}(x)$. The principal of virtual work is applied using:

$$\delta W = \sum_i \int (\hat{\sigma}_i \varepsilon_i)\, dV_i = 0, \tag{20}$$

where i represents the quantities listed in table 1 for each solution. The plane strain constitutive equation for material κ is governed by:

$$\left\{ \begin{array}{c} \varepsilon_{\kappa 11}(x) \\ \varepsilon_{\kappa 22}(x) \\ \gamma_{\kappa 12}(x) \end{array} \right\} = \left[\begin{array}{ccc} \frac{1-\nu_{\kappa 13}\,\nu_{\kappa 31}}{E_{\kappa 11}} & -\frac{\nu_{\kappa 23}\,\nu_{\kappa 31}+\nu_{\kappa 21}}{E_{\kappa 22}} & 0 \\ -\frac{\nu_{\kappa 13}\,\nu_{\kappa 32}+\nu_{\kappa 12}}{E_{\kappa 11}} & \frac{1-\nu_{\kappa 23}\,\nu_{\kappa 32}}{E_{\kappa 22}} & 0 \\ 0 & 0 & \frac{1}{G_{\kappa 12}} \end{array} \right] \left\{ \begin{array}{c} \sigma_{\kappa 11}(x) \\ \sigma_{\kappa 22}(x) \\ \tau_{\kappa 12}(x) \end{array} \right\} + \left[\begin{array}{c} \alpha_{\kappa 33}\,\nu_{\kappa 31} + \alpha_{\kappa 11} \\ \alpha_{\kappa 33}\,\nu_{\kappa 32} + \alpha_{\kappa 22} \\ 0 \end{array} \right] \Delta T \tag{21}$$

Eq. (20) applies for an arbitrary virtual stress $\hat{\sigma}_{a11}(x)$. The field equations and boundary terms of the solution becomes apparent when integration of Eq. (20) is performed by parts.

Shape Functions and Derivatives Within the Bonded Region

The shape functions and their derivatives are expressed with the following equations:

$$\begin{aligned}
\frac{N_a\left(\bar{x},\bar{\bar{\phi}}_P\right)}{l_e\bar{\bar{\Phi}}_a} =& -\left(1-\nu_{a13}\nu_{a31}\right)\left(\frac{e^{-\bar{\lambda}_3\bar{x}}\bar{\bar{D}}\left(\bar{\bar{\phi}}_P\right)}{\bar{\lambda}_3}+\frac{-e^{\bar{\lambda}_3\bar{x}}\bar{\bar{C}}\left(\bar{\bar{\phi}}_P\right)}{\bar{\lambda}_3}+\frac{e^{-\bar{\lambda}_1\bar{x}}\bar{\bar{B}}\left(\bar{\bar{\phi}}_P\right)}{\bar{\lambda}_1}+\frac{-e^{\bar{\lambda}_1\bar{x}}\bar{\bar{A}}\left(\bar{\bar{\phi}}_P\right)}{\bar{\lambda}_1}+\frac{\bar{x}}{\bar{\gamma}}\right)\\
&+\bar{x}\frac{\Theta}{\theta_{\Delta T}}\left(1-\bar{\bar{\phi}}_P\right)\left(\alpha_{a33}\nu_{a31}+\alpha_{a11}\right),\\
\frac{N_c\left(\bar{x},\bar{\bar{\phi}}_P\right)}{l\bar{\bar{\Phi}}_c} =& \frac{E_{a11}t_a\left(1-\nu_{c13}\nu_{c31}\right)}{2E_{c11}t_c}\left(\frac{e^{-\bar{\lambda}_3\bar{x}}\bar{\bar{D}}\left(\bar{\bar{\phi}}_P\right)}{\bar{\lambda}_3}-\frac{e^{\bar{\lambda}_3\bar{x}}\bar{\bar{C}}\left(\bar{\bar{\phi}}_P\right)}{\bar{\lambda}_3}+\frac{e^{-\bar{\lambda}_1\bar{x}}\bar{\bar{B}}\left(\bar{\bar{\phi}}_P\right)}{\bar{\lambda}_1}-\frac{e^{\bar{\lambda}_1\bar{x}}\bar{\bar{A}}\left(\bar{\bar{\phi}}_P\right)}{\bar{\lambda}_1}\right)\\
&+\frac{\bar{x}\left(1-\nu_{c13}\nu_{c31}\right)}{E_{c11}t_c}\left(\bar{\bar{\phi}}_P\frac{\Theta}{\theta_P}+\frac{E_{a11}t_a}{2\bar{\gamma}}\right)\\
&+\bar{x}\frac{\Theta}{\theta_{\Delta T}}\left(1-\bar{\bar{\phi}}_P\right)\left(\alpha_{c33}\nu_{c31}+\alpha_{c11}\right).
\end{aligned} \tag{22}$$

Model information

Table 4: Assumed material properties in continuum and UEL solutions (moduli in GPa, expansion coeffs. in $\mu\varepsilon\cdot\,^{\circ}\mathrm{C}^{-1}$)

Material	Aluminum	Titanium	AS4/3501-6 (0°)	FM300
E_{11}	70	110	148	1.98
E_{22}	70	110	10.6	1.98
E_{33}	70	110	10.6	1.98
G_{12}	26.3	41.4	5.61	0.71
G_{13}	26.3	41.4	5.61	0.71
G_{23}	26.3	41.4	3.17	0.71
ν_{12}	0.33	0.33	0.30	0.40
ν_{13}	0.33	0.33	0.30	0.40
ν_{23}	0.33	0.33	0.59	0.40
α_{11}	23	9	-0.8	20
α_{22}	23	9	29	20
α_{33}	23	9	29	20

System parameters in terms of material properties and loads

The following variables are used in the text in order to facilitate compact equations:

A. Dimensionless System Parameters

Table 5: Dimensionless System Parameters

Load Parameters	Material Parameters
$\bar{\phi}_P = \frac{\theta_P P}{\Theta}$	$\bar{\beta} = \frac{\theta_\beta}{\Theta}$
$\bar{\phi}_T = \frac{\theta_{\Delta T}\Delta T}{\Theta}$	$\bar{\gamma} = \frac{\theta_\gamma}{\Theta}$

B. Dimensional Material Parameters

$$\begin{aligned}
\theta_\beta =& + \frac{t_a^3}{24l^2}\left[\frac{(\nu_{a12}+\nu_{a13}\nu_{a32})}{E_{a11}} + \frac{(\nu_{a21}+\nu_{a23}\nu_{a31})}{E_{a22}}\right] \\
& - \frac{t_a^2 t_c}{24l^2}\left[\frac{(\nu_{c12}+\nu_{c13}\nu_{c32})}{E_{c11}} + \frac{(\nu_{c21}+\nu_{c23}\nu_{c31})}{E_{c22}}\right] \\
& + \frac{t_a^2}{4l^2 E_{a11}}\left(\frac{t_b}{1}(\nu_{a12}+\nu_{a13}\nu_{a32}) + \frac{t_c}{2}(\nu_{a12}+\nu_{a13}\nu_{a32})\right) \\
& + \frac{t_a^2}{4l^2 E_{a22}}\left(\frac{t_b}{1}(\nu_{a21}+\nu_{a23}\nu_{a31}) + \frac{t_c}{2}(\nu_{a21}+\nu_{a23}\nu_{a31})\right) \\
& - \frac{t_a^2}{8l^2}\left[\frac{t_c}{3G_{c11}} + \frac{t_b}{G_{b11}}\right] \\
\theta_\gamma =& \frac{t_a^2}{4E_{c11}t_c}(1-\nu_{c13}\nu_{c31}) + \frac{t_a}{2E_{a11}}(1-\nu_{a13}\nu_{a31})
\end{aligned} \tag{23}$$

C. Dimensional Load Parameters

$$\begin{aligned}
\theta_{\Delta T} =& \frac{t_a}{2E_{a11}}(\alpha_{a11}-\alpha_{c11}+\alpha_{a33}\nu_{a31}-\alpha_{c33}\nu_{c31}) \\
\theta_P =& -\frac{t_a}{2t_c E_{a11}E_{c11}}(1-\nu_{c13}\nu_{c31})
\end{aligned} \tag{24}$$

D. Dimensional System Parameter

$$\begin{aligned}
\Theta =& + (1-\nu_{a23}\nu_{a32})\frac{t_a^3}{8l^4 E_{a22}}\left[\frac{t_a^2}{30} + \frac{t_a t_c}{6} + \frac{t_c^2}{4} + \frac{t_a t_b}{3} + \frac{t_b t_c}{1} + \frac{t_b^2}{1}\right] \\
& + (1-\nu_{b23}\nu_{b32})\frac{t_a^2 t_b}{4l^4 E_{b22}}\left[\frac{t_c^2}{4} + \frac{t_b^2}{3} + \frac{t_b t_c}{2}\right] \\
& + (1-\nu_{c23}\nu_{c32})\frac{t_a^2 t_c^3}{80l^4 E_{c22}}
\end{aligned} \tag{25}$$

E. Intermediate variables

$$\begin{aligned}
\bar{\bar{\Phi}}_a &= \frac{\bar{\lambda}_1\bar{\lambda}_3 e^{\bar{\lambda}_3+\bar{\lambda}_1}}{\bar{\bar{\Xi}}_a}, \\
\bar{\bar{\Phi}}_c &= \frac{\bar{\lambda}_1\bar{\lambda}_3 e^{\bar{\lambda}_3+\bar{\lambda}_1}}{\bar{\bar{\Xi}}_c}.
\end{aligned} \tag{26}$$

$$
\begin{aligned}
\bar{\bar{\Xi}}_a =& + l_e\bar{\lambda}_1\left(1-\nu_{a13}\nu_{a31}\right)\left(e^{\bar{\lambda}_3+\bar{\lambda}_1}-e^{\bar{\lambda}_1}\right)\bar{\bar{D}}\left(\bar{\bar{\phi}}_P\right)\\
&+ l_e\bar{\lambda}_1\left(1-\nu_{a13}\nu_{a31}\right)\left(e^{2\bar{\lambda}_3+\bar{\lambda}_1}-e^{\bar{\lambda}_3+\bar{\lambda}_1}\right)\bar{\bar{C}}\left(\bar{\bar{\phi}}_P\right)\\
&+ l_e\bar{\lambda}_3\left(1-\nu_{a13}\nu_{a31}\right)\left(e^{\bar{\lambda}_3+\bar{\lambda}_1}-e^{\bar{\lambda}_3}\right)\bar{\bar{B}}\left(\bar{\bar{\phi}}_P\right)\\
&+ l_e\bar{\lambda}_3\left(1-\nu_{a13}\nu_{a31}\right)\left(e^{\bar{\lambda}_3+2\bar{\lambda}_1}-e^{\bar{\lambda}_3+\bar{\lambda}_1}\right)\bar{\bar{A}}\left(\bar{\bar{\phi}}_P\right)\\
&- l_e\bar{\lambda}_1\bar{\lambda}_3 e^{\bar{\lambda}_3+\bar{\lambda}_1}\left(\frac{\left(1-\nu_{a13}\nu_{a31}\right)}{\bar{\gamma}}-\frac{\Theta}{\theta_{\Delta T}}\left(1-\bar{\bar{\phi}}_P\right)\left(\alpha_{a11}+\alpha_{a33}\nu_{a31}\right)\right),\\
\bar{\bar{\Xi}}_c =& -\frac{E_{a11}t_a}{2E_{c11}t_c}l_e\bar{\lambda}_1\left(1-\nu_{c13}\nu_{c31}\right)\left(e^{\bar{\lambda}_1}+e^{\bar{\lambda}_3+\bar{\lambda}_1}\right)\bar{\bar{D}}\left(\bar{\bar{\phi}}_P\right)\\
&-\frac{E_{a11}t_a}{2E_{c11}t_c}l_e\bar{\lambda}_1\left(1-\nu_{c13}\nu_{c31}\right)\left(e^{2\bar{\lambda}_3+\bar{\lambda}_1}-e^{\bar{\lambda}_3+\bar{\lambda}_1}\right)\bar{\bar{C}}\left(\bar{\bar{\phi}}_P\right)\\
&-\frac{E_{a11}t_a}{2E_{c11}t_c}l_e\bar{\lambda}_3\left(1-\nu_{c13}\nu_{c31}\right)\left(e^{\bar{\lambda}_3}+e^{\bar{\lambda}_3+\bar{\lambda}_1}\right)\bar{\bar{B}}\left(\bar{\bar{\phi}}_P\right)\\
&-\frac{E_{a11}t_a}{2E_{c11}t_c}l_e\bar{\lambda}_3\left(1-\nu_{c13}\nu_{c31}\right)\left(e^{\bar{\lambda}_3+2\bar{\lambda}_1}-e^{\bar{\lambda}_3+\bar{\lambda}_1}\right)\bar{\bar{A}}\left(\bar{\bar{\phi}}_P\right)\\
&+\frac{l_e\bar{\lambda}_1\bar{\lambda}_3 e^{\bar{\lambda}_3+\bar{\lambda}_1}}{2E_{c11}t_c}\left(\frac{\left(1-\nu_{c13}\nu_{c31}\right)}{\bar{\gamma}}\left(E_{a11}t_a+2\bar{\gamma}\bar{\bar{\phi}}_P\frac{\Theta}{\theta_P}\right)\right)\\
&+\frac{l_e\bar{\lambda}_1\bar{\lambda}_3 e^{\bar{\lambda}_3+\bar{\lambda}_1}}{2E_{c11}t_c}\left(\frac{\Theta}{\theta_{\Delta T}}\left(1-\bar{\bar{\phi}}_P\right)\left(\alpha_{c11}+\alpha_{c33}\nu_{c31}\right)\right).
\end{aligned}
\tag{27}
$$

F. μ parameters for the basis coefficients

The μ values of Eq. (10) are given by:

$$
\begin{aligned}
\mu_{A_T} =& \frac{\bar{\lambda}_3\left(e^{\bar{\lambda}_3}-1\right)}{\bar{\gamma}}\\
\mu_{B_T} =& \frac{e^{\bar{\lambda}_1}\bar{\lambda}_3\left(e^{\bar{\lambda}_3}-1\right)}{\bar{\gamma}}\\
\mu_{C_T} =& -\frac{\bar{\lambda}_1\left(e^{\bar{\lambda}_1}-1\right)}{\bar{\gamma}}\\
\mu_{D_T} =& -\frac{\bar{\lambda}_1\left(e^{\bar{\lambda}_1}-1\right)e^{\bar{\lambda}_3}}{\bar{\gamma}}\\
\mu_{A_P} =& -\left(\bar{\lambda}_3 e^{2\bar{\lambda}_3+\bar{\lambda}_1}-\bar{\lambda}_1 e^{2\bar{\lambda}_3+\bar{\lambda}_1}+2\bar{\lambda}_1 e^{\bar{\lambda}_3}-e^{\bar{\lambda}_1}\bar{\lambda}_3-\bar{\lambda}_1 e^{\bar{\lambda}_1}\right)\\
\mu_{B_P} =& e^{\bar{\lambda}_1}\left(-2\bar{\lambda}_1 e^{\bar{\lambda}_3+\bar{\lambda}_1}+\bar{\lambda}_3 e^{2\bar{\lambda}_3}+\bar{\lambda}_1 e^{2\bar{\lambda}_3}-\bar{\lambda}_3+\bar{\lambda}_1\right)\\
\mu_{C_P} =& \frac{\bar{\lambda}_1\left(\bar{\lambda}_3 e^{\bar{\lambda}_3+2\bar{\lambda}_1}-\bar{\lambda}_1 e^{\bar{\lambda}_3+2\bar{\lambda}_1}+\bar{\lambda}_3 e^{\bar{\lambda}_3}+\bar{\lambda}_1 e^{\bar{\lambda}_3}-2e^{\bar{\lambda}_1}\bar{\lambda}_3\right)}{\bar{\lambda}_3}\\
\mu_{D_P} =& -\frac{\bar{\lambda}_1 e^{\bar{\lambda}_3}\left(2\bar{\lambda}_3 e^{\bar{\lambda}_3+\bar{\lambda}_1}-e^{2\bar{\lambda}_1}\bar{\lambda}_3-\bar{\lambda}_3-\bar{\lambda}_1 e^{2\bar{\lambda}_1}+\bar{\lambda}_1\right)}{\bar{\lambda}_3}\\
\mu_1 =& \bar{\lambda}_3 e^{\bar{\lambda}_3+\bar{\lambda}_1}-\bar{\lambda}_1 e^{\bar{\lambda}_3+\bar{\lambda}_1}+\bar{\lambda}_3 e^{\bar{\lambda}_3}+\bar{\lambda}_1 e^{\bar{\lambda}_3}-e^{\bar{\lambda}_1}\bar{\lambda}_3-\bar{\lambda}_3-\bar{\lambda}_1 e^{\bar{\lambda}_1}+\bar{\lambda}_1\\
\mu_2 =& \bar{\lambda}_3 e^{\bar{\lambda}_3+\bar{\lambda}_1}-\bar{\lambda}_1 e^{\bar{\lambda}_3+\bar{\lambda}_1}-\bar{\lambda}_3 e^{\bar{\lambda}_3}-\bar{\lambda}_1 e^{\bar{\lambda}_3}+e^{\bar{\lambda}_1}\bar{\lambda}_3-\bar{\lambda}_3+\bar{\lambda}_1 e^{\bar{\lambda}_1}+\bar{\lambda}_1\\
\mu_3 =& \frac{E_{c11}\bar{\lambda}_3 t_b^3 t_c\left(\nu_{b23}\nu_{b32}-1\right)}{3E_{b22}l^4\left(\nu_{c13}\nu_{c31}-1\right)}
\end{aligned}
\tag{28}
$$

Acknowledgments

This work was supported by the Space Vehicle Technology Institute under grant NCC3-989 jointly funded by NASA and the Department of Defense. It is managed within the NASA Constellation University Institutes Project, with Claudia Meyer as the project manager. P.A. Gustafson also extends gratitude to all contributors to the Maxima project, which was used for symbolic calculations.

References

[1]Gustafson, P. A., Bizard, A., and Waas, A. M., "Dimensionless parameters in symmetric double lap joints: an orthotropic solution for thermomechanical loading," *Proceedings of the AIAA/ASME/ASCE/AHS/ASC 47th Structures, Structural Dynamics, and Materials Conference, May 1-4 2006, Newport RI*, No. 2006-1959, American Institute of Aeronautics and Astronautics, 2006.

[2]Gustafson, P. A., Bizard, A., and Waas, A. M., "Dimensionless parameters in symmetric double lap joints: An orthotropic solution for thermomechanical loading," *International Journal of Solids and Structures*, 2007 In Press.

[3]Gustafson, P. A. and Waas, A. M., "A macroscopic joint finite element for a symmetric double lap joint," *Proceedings of the American Society of Composites 21st Annual Technical Conference*, No. 204, American Society of Composites, Sept 2006.

[4]Adams, R., Comyn, J., and Wake, W., *Structural Adhesive Joints in Engineering*, Chapman and Hall, 1997.

[5]Oterkus, E., Madenci, E., Smeltzer III, S., and Ambur, D., "Thermo-Mechanical Analysis of Bonded Cylindrically Curved Composite Shell Structures," *Proceedings of the AIAA/ASME/ASCE/AHS/ASC 47th Structures, Structural Dynamics, and Materials Conference, May 1-4, Newport, RI*, No. 2006-1963, American Institute of Aeronautics and Astronautics, 2006.

[6]Wooley, G. R. and Carver, D. R., "Stress Concentration Factors for Bonded Lap Joints," *J. Aircraft*, Vol. 8, 1971, pp. 817–820.

[7]Adams, R. D. and Peppiatt, N. A., "Stress Analysis of Adhesive-Bonded Lap Joints," *J. Strain Analysis*, Vol. 9, No. 3, 1974, pp. 185–196.

[8]Kafkalidis, M. S. and Thouless, M. D., "The effects of geometry and material properties on the fracture of single lap-shear joints," *International Journal of Solids and Structures*, Vol. 39, No. 17, Aug. 2002, pp. 4367–4383.

[9]Xie, D., Waas, A. M., Shahwan, K. W., Schroeder, J. A., and Boeman, R. G., "Fracture criterion for kinking cracks in a tri-material adhesively bonded joint under mixed mode loading," *Engineering Fracture Mechanics*, Vol. 72, No. 16, Nov. 2005, pp. 2487–2504.

[10]Li, S., Thouless, M., Waas, A., Schroeder, J., and Zavattieri, P., "Use of a cohesive-zone model to analyze the fracture of a fiber-reinforced polymer-matrix composite," *Composites Science and Technology*, Vol. 65, No. 3-4, March 2005, pp. 537–549.

[11]Li, S., Thouless, M., Waas, A., Schroeder, J., and Zavattieri, P., "Competing failure mechanisms in mixed-mode fracture of an adhesively bonded polymer-matrix composite," *International Journal of Adhesion and Adhesives*, Vol. 26, No. 8, Dec. 2006, pp. 609–616.

[12]Valoroso, N. and Champaney, L., "A damage-mechanics-based approach for modelling decohesion in adhesively bonded assemblies," *Engineering Fracture Mechanics*, Vol. In Press, Corrected Proof, 2006, pp. –.

[13]Xie, D. and Waas, A. M., "Discrete cohesive zone model for mixed-mode fracture using finite element analysis," *Engineering Fracture Mechanics*, Vol. 73, No. 13, Sept. 2006, pp. 1783–1796.

[14]Weerts, U. and Kossira, H., "Mixed mode fracture characterization of adhesive joints," *ICAS Congress*, International Congress Aeronautical Sciences, 2000, Harrogate (GB), pp 451.1-451.9.

[15]Aydemir, A. and Gunay, D., "The fuzzy finite element stress analysis of adhesive-bonded single lap joints," *Turkish J. Eng. Env. Sci*, 2003, pp. 121–127.

[16]Koutsourelakis, P., Kuntiyawichai, K., and Schueller, G., "Effect of material uncertainties on fatigue life calculations of aircraft fuselages: A cohesive element model," *Engineering Fracture Mechanics*, Vol. 73, No. 9, June 2006, pp. 1202–1219.

[17]Gillespie, Jr, J. W., Carlsson, L. A., and Pipes, R. B., "Finite element analysis of the end notched flexure specimen for measuring mode II fracture toughness," *Composites Science and Technology*, Vol. 27, No. 3, 1986, pp. 177–197.

[18]Wang, J. T., Raju, I. S., and Sleight, D. W., "Fracture mechanics analyses of composite skin-stiffener debond configurations with shell elements," No. 94-1389 -CP, 1994.

[19]Glaessgen, E., Raju, I., and C.C. Poe, J., "Fracture mechanics analysis of stitched stiffener-skin debonding," No. 98-2022, 1998.

[20]Krueger, R., "Virtual crack closure technique: History, approach, and applications," *Applied Mechanics Reviews*, Vol. 57, No. 2, 2004, pp. 109–143.

[21]Xie, D., Waas, A. M., Shahwan, K. W., Schroeder, J. A., and Boeman, R. G., "Computation of Energy Release Rates for Kinking Cracks based on Virtual Crack Closure Technique," *Computer Modeling in Engineering & Sciences*, Vol. 6, 2004, pp. 515–524.

[22]Xie, D., Salvi, A. G., Waas, A. M., and Caliskan, A., "Discrete cohesive zone model to simulate static fracture in carbon fiber textile composites," *46th AIAA/ASME/ASCE/AHS/ASC Structures, Structrual Dynamics and Materials Conference*, 2005.

[23]Xie, D. and Sherrill B. Biggers, J., "Progressive crack growth analysis using interface element based on the virtual crack closure technique," *Finite Elem. Anal. Des.*, Vol. 42, No. 11, 2006, pp. 977–984.

[24]Munoz, J., Galvanetto, U., and Robinson, P., "On the numerical simulation of fatigue driven delamination with interface elements," *International Journal of Fatigue*, Vol. 28, No. 10, Oct. 2006, pp. 1136–1146.

[25]Goncalves, J. P. M., de Moura, M. F. S. F., and de Castro, P. M. S. T., "A three-dimensional finite element model for stress analysis of adhesive joints," *International Journal of Adhesion and Adhesives*, Vol. 22, No. 5, 2002, pp. 357–365.

[26]Goyal, V. K., Johnson, E. R., and Cassino, C., "Computational model for progressive failure of adhesivley bonded joints," *44th AIAA/ASME/ASCE/AHS/ASC Structures, Structrual Dynamics and Materials Conference*, 2003.

[27]ABAQUS, Inc, *ABAQUS User Manual v6.5*, Electronic Version, 2006.

[28]Sandia National Laboratory, *Tahoe User Guide*, 3rd ed., May 2003.

[29]Oterkus, E., Barut, A., Madenci, E., Smeltzer III, S., and Ambur, D., "Nonlinear analysis of bonded composite single-lap joints," *Proceedings of the AIAA/ASME/ASCE/AHS/ASC 45th Structures, Structural Dynamics, and Materials Conference, April 19-22, Palm Springs, CA*, No. 2004-1560, American Institute of Aeronautics and Astronautics, 2004.

[30]Oterkus, E., Madenci, E., Smeltzer III, S., and Ambur, D., "Nonlinear analysis of bonded composite tubular lap joints," *Proceedings of the AIAA/ASME/ASCE/AHS/ASC 46th Structures, Structural Dynamics, and Materials Conference, April 18-21, Austin, TX*, No. 2005-2380, American Institute of Aeronautics and Astronautics, 2005.

[31]Smeltzer III, S. S. and Lundgren, E., "Analytical and Numerical Results for an Adhesively Bonded Joint Subjected to Pure Bending," *Proceedings of the AIAA/ASME/ASCE/AHS/ASC 47th Structures, Structural Dynamics, and Materials Conference, May 1-4 2006, Newport RI*, No. 2006-1960, American Institute of Aeronautics and Astronautics, 2006.

[32]Bednarcyk, B. A., Zhang, J., Collier, C. S., Bansal, Y., and Pindera, M. J., "Analysis tools for adhesively bonded composite joints, Part 1: Higher-order theory," *AIAA JOURNAL*, Vol. 44, No. 1, Jan. 2006, pp. 171–180.

[33]Gustafson, P. A. and Waas, A. M., "A macroscopic finite element for a symmetric doublelap joint subjected to mechanical and thermal loading," *Computer Methods in Applied Mechanics and Engineering* To Be Submmitted, 2007.

[34]Kilic, B., Madenci, E., and Ambur, D., "Global-local finite element analysis of bonded single-lap joints," *45th AIAA/ASME/ASCE/AHS/ASC Structures, Structrual Dynamics and Materials Conference, April 19-22, Palm Springs, CA*, 2004, pp. 1–13.

[35]Hart-Smith, L., "Adhesive-Bonded Double-Lap Joints," *NASA Contractor Report 112235*, 1973.

[36]Zhang, J., Collier, C., Bansal, Y., Bednarcyk, B. A., and Pindera, M.-J., "Analysis of Adhesively Bonded Composite Joints using a higher-order theory," *45th AIAA/ASME/ASCE/AHS/ASC Structures, Structrual Dynamics and Materials Conference, April 19-22, Palm Springs CA*, 2004, pp. 1–16.

[37]Davies, G., *Virtual work in structural analysis*, John Wiley & Sons, 1982.

[38]Cook, R. D., Malkus, D. S., and Plesha, M. E., *Concepts and applications of finite element analysis*, John Wiley & Sons, 1989.

[39]ASTM International, *ASTM D 3528-96 Standard Test Method for Strength Properties of Double Lap Shear Adhesive Joints by Tension Loading*.

[40]Herakovich, C. T., *Mechanics of fibrous composites*, John Wiley and Sons, Inc, 1998.